OPEN ACCESS
IOP Publishing | International Atomic Energy Agency Nuclear Fusion

Nucl. Fusion **62** (2022) 086004 (12pp) https://doi.org/10.1088/1741-4326/ac6d6a

Developing a physics understanding of the quasi-continuous exhaust regime: pedestal profile and ballooning stability analysis

L. Radovanovic[1,*], M. Dunne[2], E. Wolfrum[2], G. Harrer[1], M. Faitsch[2], R. Fischer[2], F. Aumayr[1], the ASDEX Upgrade Team[a] and the EUROfusion MST1 Team[b]

[1] Institute of Applied Physics, TU Wien, Fusion@ÖAW, Wiedner Hauptstr. 8-10, 1040 Vienna Austria
[2] Max Planck Institute for Plasma Physics, Bolzmannstraße 2, 85748 Garching, Germany

E-mail: radovanovic@iap.tuwien.ac.at

Received 13 January 2022, revised 6 April 2022
Accepted for publication 6 May 2022
Published 24 May 2022

Abstract

It has been experimentally observed that at ASDEX Upgrade (AUG) plasmas at relatively high shaping, an increase of gas fuelling corresponds to an increase of the frequency and intensity of the type-I edge localised modes (ELMs). At high enough fuelling, the plasma enters the quasi continuous exhaust (QCE) regime. We have performed ideal ballooning $n \rightarrow \infty$ stability analysis on four AUG discharges, comparing the type-I ELM dominated phases, with the phases that are in the QCE regime. The results of this study show that as the gas puff increases, the plasma gets more ballooning unstable in the pedestal region, especially very close to the separatrix, at the pedestal bottom. On the contrary, in the middle of the pedestal, the discharges are more ballooning stable. Here the locally negative magnetic shear has a stabilising effect on ballooning modes, allowing access to the second stability region. Our analysis of the ballooning stability and the confinement factor H_{98} suggest that with optimisation of the pedestal shape, good confinement without type-I ELMs can be achieved. Necessary ingredients are that the region of the highest pressure gradient is not ideal ballooning limited, while the pedestal bottom is ballooning unstable. Ideal stability analysis of 36 simulated ITER profiles shows that, similarly to the experimental cases from AUG, a high pedestal top pressure can be maintained concomitant with a ballooning instability at the pedestal bottom, making QCE a promising scenario.

Keywords: magnetic confinement, pedestal stability, QCE regime, small ELMs, ballooning modes

(Some figures may appear in colour only in the online journal)

[*] Author to whom any correspondence should be addressed.
[a] See Meyer *et al* 2019 (https://doi.org/10.1088/1741-4326/ab18b8) for the ASDEX Upgrade Team.
[b] See Labit *et al* 2019 (https://doi.org/10.1088/1741-4326/ab2211) for the EUROfusion MST1 Team.

1. Introduction

The high confinement mode (H-mode) [1], which is characterised by steep pressure gradients at the plasma edge and associated edge localised modes (ELMs), is the foreseen operational regime for future fusion devices [2, 3]. It has been shown that when scaled to larger tokamaks, type-I ELMs are no longer expected to be tolerable because of high heat and particle loads on plasma facing components [4, 5].

ELM mitigation strategies or alternative operational regimes are therefore considered for reactor relevant scenarios. It has been shown that type-I ELMs occur less frequently and with lower magnitude if small ELMs appear simultaneously [6]. Since the distinction between type-II ELMs [7, 8], type-III ELMs [9] and grassy ELMs [10] is not always definite, they have been commonly referred to as small ELMs [6, 11–13]. The regime on ASDEX Upgrade (AUG) in which small ELMs completely replace type-I ELMs is called the quasi continuous exhaust (QCE) regime [14]. A significant advantage of this regime is that transport to the scrape-off layer (SOL) takes the form of steady fluctuations instead of large ELMy bursts, while keeping a good plasma confinement. The QCE regime has also been correlated with increased filamentary transport in the SOL [15]. Consequently, the power fall-off length is increased and the peak power load on the divertor plates is significantly reduced [14].

Type-I ELMs are generally well described and predicted by the peeling-ballooning theory [16]. However, the experimentally observed small ELMs have not yet been so robustly linked to a theoretical model. In the peeling ballooning theoretical frame, type-II ELMs were explained by a change of the operational stability point [17]: the reduced maximal normalised pressure gradient and a reduced bootstrap current put the operational point close to the high-n ballooning boundary. However, this picture cannot explain why type-I ELMs and small ELMs can occur simultaneously.

Recent theoretical studies have suggested that a pure ballooning mechanism could be responsible for small ELMs and the related filaments in the SOL [18, 19]. Newer research on AUG [6] investigates the significance of the separatrix density for the QCE regime, revealing the local characteristics of small ELMs, moreover indicating their ballooning nature. Other experimental studies on AUG and JET have shown a close relationship between the separatrix density and ballooning stability [20].

A model presented in [6] characterises the QCE regime as a regime in which localised ballooning modes provide sufficient transport to modify the shape of the pedestal profile such that it is stable against global type-I ELMs. With ballooning transport as the main suspect behind the increased transport, we investigate the stability of the plasma edge with respect to local ballooning in four discharges containing large and small ELMs. The QCE and small ELM regimes on AUG are mainly established at high density (high fuelling rates) and high shaping [6–8, 21]. Therefore, we analyse discharges which are highly shaped compared to typical operation on AUG, with an average plasma triangularity of approximately 0.4 at different plasma current I_p with a density variation achieved by changing the D_2 fuelling, described in section 2. We use the code HELENA [22, 23] to apply ideal $n \to \infty$ MHD analysis as a proxy for the onset of a ballooning mode and investigate in detail the stabilising effects of the magnetic shear and the destabilising effects of the pressure gradient. In section 3 the analysis results of the discharges show that the pedestal bottom is ballooning unstable in phases with small ELMs. Good confinement, however, is correlated with access to second stability in the middle of the pedestal. In section 4 the workflow is applied to a range of test profiles along with the ITER geometry and machine parameters ($I_p = 15$ MA, $B_T = 5.3$ T) to see if this plasma shape and edge safety factor profile could potentially create conditions similar to those observed in the QCE regime of AUG. Finally, the results are discussed in section 5.

2. Experiments and analysis methods

2.1. Influence of fuelling variation

In experiments performed on AUG, it is observed that the dominant ELM type is strongly influenced by the level of D_2 puff [6]. In the following, four discharges are analysed to illustrate this effect. The triangularity is high throughout all four discharges; the upper triangularity has values $0.27 < \delta^u < 0.32$ and the lower triangularity $0.42 < \delta^l < 0.47$. Figure 1 shows the time traces of the outer divertor shunt current $I_{polSOLa}$, which is used as an ELM indicator. The 100 ms time windows in which further analysis is performed are marked with blue (low fuelling, type-I ELMs) and orange (high fuelling, QCE) bars, and zoomed shunt current time traces are depicted in the right panels in the respective colours for those time windows. The D_2 gas puff level is shown in the left panels as a green line.

Figure 1(a) shows discharge #35562 with a higher plasma current ($I_p = 1$ MA). In this discharge the final high shaping is reached at 3 s, in the other three discharges the final shape is already achieved at 2 s. Between 3 s and 5 s, in the high fuelling phase, the type-I ELM size is reduced and small ELMs are more frequent. After the reduction in fuelling at 5 s the plasma is dominated by larger type-I ELMs.

Figures 1(b) and (c) show discharges at medium plasma current ($I_p = 0.8$ MA) at different toroidal magnetic fields, with similar heating power. Discharge #36080 (figure 1(b)) has a stepwise decrease, and #36165 (figure 1(c)) has a stepwise increase in the D_2 puffing level. In the case with the gas increase (figure 1(c)), the discharge has low gas puff and large type-I ELMs in the beginning of the discharge. As the fuelling increases, small ELMs appear between the type-I ELMs. Simultaneously, type-I ELMs show weakening intensity and a frequency that remains at approximately 120 Hz in the first phase of the discharge and starts dropping at 4 s. In the high gas puff phase, after 5 s, large ELMs completely cease and the plasma enters the QCE regime. In the case with the

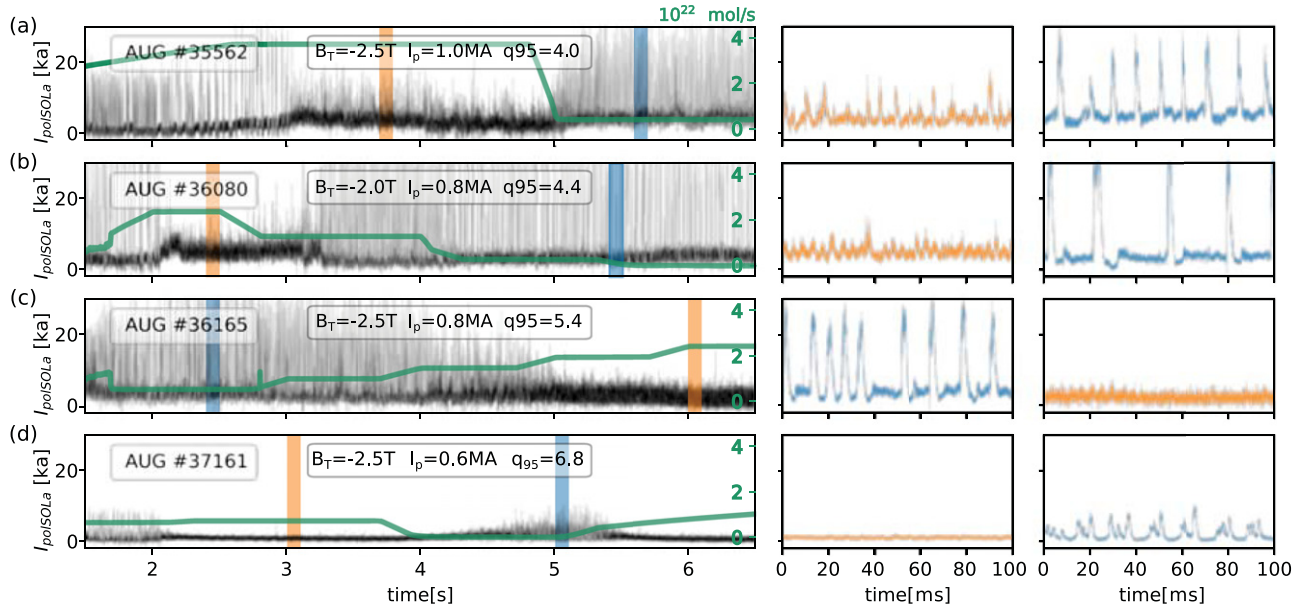

Figure 1. Time traces of outer divertor current I_{polSOLa} for discharges with gas puff variation. A discharge with high plasma current is shown in (*a*), medium plasma current are in (*b*) and (*c*), low plasma current in (*d*). Plasma current I_{p}, toroidal magnetic field B_{T} and safety factor q (in ascending order) of each discharge are indicated in text boxes. Blue and orange bars represent the 100 ms time windows with low and high D_2 puff, respectively. The marked time windows in the left panels are zoomed in the middle and right panels, marked with corresponding colours. The green traces in the left panels show the amount of D_2 puff, with the scale on the right side of the plots.

stepwise decrease of D_2 puff (figure 1(*b*)), the plasma shows analogous behaviour corresponding to the change in fuelling.

Discharge #37161 (figure 1(*d*)) has low plasma current ($I_{\mathrm{p}} = 0.6$ MA) and high q_{95}, a condition in which the QCE regime tends to be more easily achieved, also at lower gas puffing. After the start-up phase, from 2 s on, the gas puff is held constant and the QCE regime is established. At 3.8 s the gas puff is decreased to zero. This is followed by a slightly delayed reappearance of larger ELMs around 5 s. At 5.5 s the fuelling is at its initial level and the QCE is re-established.

The four discharges have high heating power, ranging between 5 MW and 11 MW and reactor relevant β_N ($\beta_N = 1.4$–2.4) with different fuelling patterns (step—up, step—down, shorter and more severe reduction) and at different plasma currents and values of safety factor q. Therefore, they cover a wide range of operational regimes in QCE, and have been considered suitable for the following ideal ballooning stability analysis.

2.2. Workflow

Electron density and temperature measurements from AUG diagnostics (Thomson scattering, electron cyclotron emission, deuterium cyanide laser interferometry and lithium beam) and a reconstructed equilibrium are used as input for the integrated data analysis (IDA) [24] to obtain the electron density and temperature profiles.

Figures 2(*a*)–(*c*) shows an example of IDA reconstructed edge kinetic profiles plotted against the normalised radius ρ for discharge #36165. Profiles are taken every 5 ms in the time windows marked in figure 1(*a*). The full line is a median for the given window, and the shaded area represents a 95% temporal confidence interval. In the high D_2 puff phase, the electron temperature decreases (figure 2(*a*)) while the electron density (figure 2(*b*)) increases relative to the phase with low D_2 puff, which leads to small but significant changes in electron pressure profile (figure 2(*c*)) at the pedestal top and bottom. In the high fuelling phase, the pressure gradient itself is very similar, however the profile is shifted to larger radii, the pressure close to the separatrix is higher and the steepest region narrower. Because the pressure gradient is taken as an input for the ballooning analysis, any possible effect of relative variations in temperature vs density only come in as higher-order effects, described in the following.

Both increased density and decreased temperature lead to higher collisionality. This causes lower bootstrap current and therefore lower flux surface averaged toroidal current density (figure 2(*d*)), which changes the equilibrium. Furthermore, higher gas puff increases the density at the separatrix, effectively shifting the pedestal outwards, which has a destabilising effect [25] and it limits the pedestal top pressure. This implies that the change in electron density has a number of consequent influences on the plasma equilibrium.

The obtained density and temperature profiles are used for a reconstruction of a more accurate equilibrium using integrated data analysis equilibrium [26]. This equilibrium provides an input for the code HELENA, namely the pressure gradient $\mathrm{d}p/\mathrm{d}r$, the diamagnetic profile and its derivative $F\mathrm{d}F/\mathrm{d}r$, with $F = RB_{\mathrm{tor}}$, and the plasma boundary. With these parameters, the Grad–Shafranov equation is numerically solved at high radial resolution, and the Suydam method [27] is applied to perform the ideal $n \to \infty$ ballooning stability analysis of the plasma.

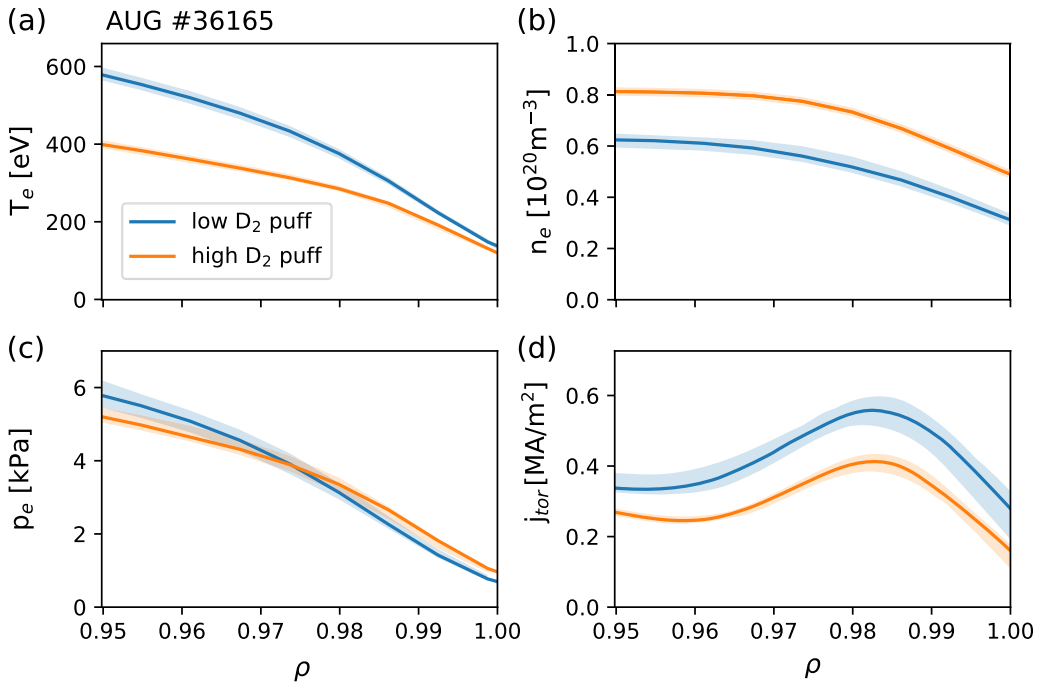

Figure 2. Reconstructed kinetic profiles at the plasma edge: electron temperature (*a*), electron density (*b*) and electron pressure (*c*). Toroidal current density is shown in (*c*). Orange lines represent the high gas puff and blue lines the low gas puff phases. Shaded areas are 95% of the temporal variation for the 100 ms time windows.

The HELENA code delivers the outputs relevant for ballooning stability: the global flux surface averaged magnetic shear s defined as

$$s = \frac{r}{q}\frac{\partial q}{\partial r} \tag{1}$$

and the experimental and critical value of the normalised pressure gradient α defined as

$$\alpha = -2\mu_0 \frac{\partial V}{\partial \psi}\frac{1}{(2\pi)^2}\left(\frac{V}{2\pi^2 R_0}\right)^{1/2}\frac{\partial p}{\partial \psi}, \tag{2}$$

where V is the plasma volume, ψ is the magnetic flux function and R_0 the large radius at the magnetic axis.

In a circular cross-section plasma, α can also be expressed as $\alpha \sim q^2/B^2 \mathrm{d}p/\mathrm{d}r$. The value of α is then varied at constant shear and background equilibrium until a ballooning instability is found, resulting in a value for α_{crit}. The relation between critical and experimental α is calculated as the marginal ballooning stability factor:

$$F_{\mathrm{marg}} = \frac{\alpha_{\mathrm{crit}}}{\alpha_{\mathrm{exp}}}. \tag{3}$$

That is, if $F_{\mathrm{marg}} > 1$ the plasma is ballooning stable and if $F_{\mathrm{marg}} < 1$ the plasma is ballooning unstable. These three parameters are first inspected for the chosen data set of the four AUG discharges, and then also for a set of predicted ITER—like profiles.

3. Ballooning stability analysis of the selected AUG pedestals

3.1. Ballooning profiles

Figure 3 shows the global magnetic shear s, the experimental and the critical normalised pressure gradient α (full and dashed lines respectively) and the ballooning stability factor F_{marg} for the time windows marked in figure 1 at the plasma edge. Temporal medians are shown as full lines, and 95% of the temporal variation is depicted as shaded areas. For better clarity, only the median values of α_{crit} are shown. Green horizontal lines in the F_{marg} plots represent the ideal ballooning stability limit.

In the first row, in all four cases the global magnetic shear is higher in the phases with high gas puffing and this effect is smallest in the discharge with low q (figure 3(*a*)) and strongest in the discharge with high q (figure 3(*d*)). The change in the gas fuelling is also reflected in the change of α_{crit}, that is, the α at which the plasma becomes ballooning unstable, shown in the second row of figure 3 as dashed line. This parameter also shows the smallest change in the high current case. As described in section 2.1, the temperature compensates for the density so that the pressure changes only slightly. Therefore, α_{exp} also stays very similar for both phases, except for the low current discharge (figure 3(*d*)), in which the experimental pressure gradient flattens in the high D_2 puff phase.

The relation between α_{crit} and α_{exp} is expressed as F_{marg} and it is plotted in the third row. There are three distinct regions in the marginal stability factor F_{marg}: closest to the separatrix, around $0.99 \lesssim \rho \lesssim 1.00$ the plasma is the closest to the

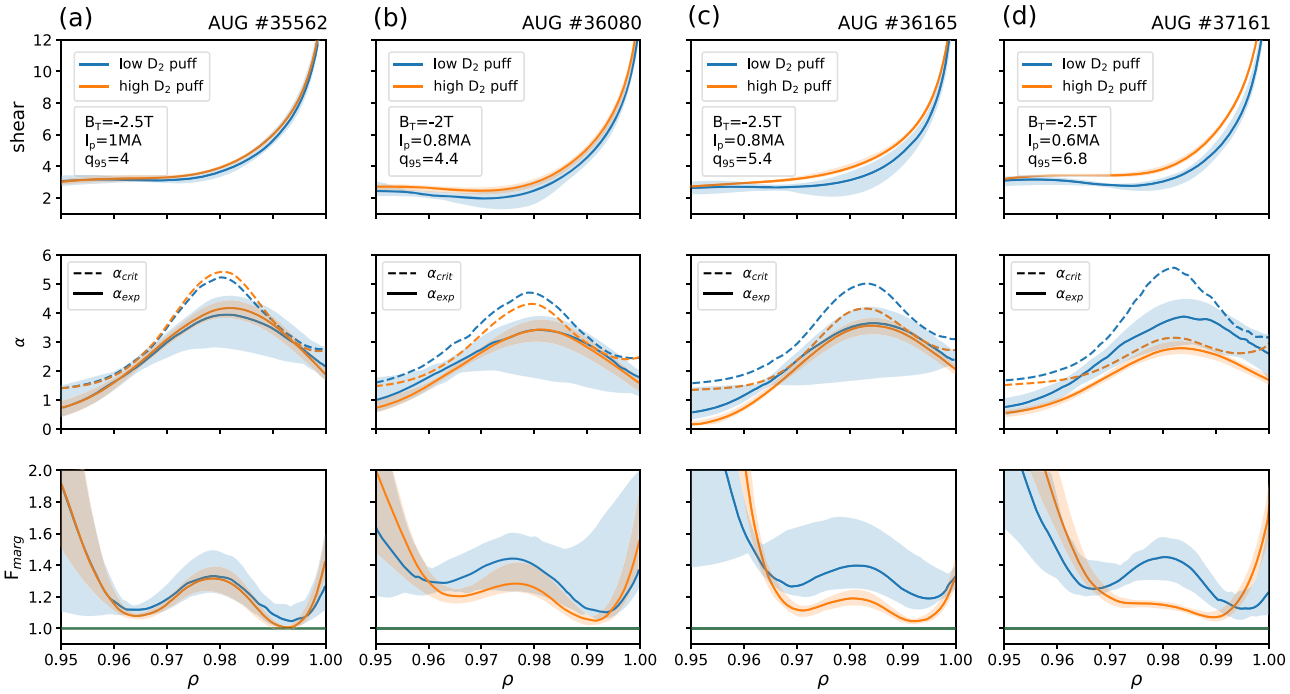

Figure 3. Radial profiles of global magnetic shear in the top panels, critical α (dashed line) and experimental α (full line) in the middle panels and ballooning stability factor F_{marg} in the bottom panels. The discharges are shown in the ascending q_{95} order. The full line represents the temporal median, and the shaded area the 95% of the temporal variation for the analysed 100 ms. Phases with the high D_2 gas puff are marked in orange, and phases with low D_2 gas puff in blue.

ideal ballooning stability limit, especially so in the phases with the high gas puffing. The pedestal middle is more stable, except for the low current discharge in the high gas puff phase (figure 3(*d*) in orange), which has a flatter pedestal middle. The region around the pedestal top at $0.96 \lesssim \rho \lesssim 0.97$ also shows closeness to the ballooning stability limit.

The data show that in all four cases the plasma is closer to the ideal ballooning stability limit in the high D_2 puff phases in which the plasma is in the QCE regime. The described discharges show lower values of F_{marg} in phases with higher global s. This is seemingly in contradiction with the simplified ballooning picture, which says that ballooning modes are stabilised by the magnetic shear. However, the magnetic shear depicted in figure 3 is the global flux surface averaged magnetic shear and the local magnetic shear can be considerably different from its global average.

3.2. Access to second stability

The stabilising term in the ballooning equation is the square of the magnetic shear. Therefore, locally negative magnetic shear would lower the flux averaged magnetic shear, but its square would still locally have the stabilising effect. In the standard AUG configurations, this mostly happens at the low field side (LFS), where ballooning modes are destabilised by the bad curvature. The normalised pressure gradient also influences the magnetic shear by increasing its poloidal variation, due to the stronger Shafranov shift, and it can effectively enhance the stabilising effect. Figure 4 shows the local shear, as defined in [28] for three poloidal angles at the LFS for the two phases depicted in figure 3(*a*). One should note that at points where the local shear (s_{loc}) changes its sign, the square value is zero, therefore, there is no stabilising effect and this contributes to the F_{marg} local minimum at the pedestal top and bottom.

The point where $s^2_{\mathrm{loc}} = 0$ is however at different radial positions depending on the poloidal angle as shown in figure 4.

The effect of the poloidally varying magnetic shear can also be depicted in the s–alpha diagram (figure 6). Typically, in the core, in the first stable region, the magnetic shear is positive at all poloidal angles (figure 6(*a*)). However, in the edge first stable region (figure 6(*b*)), high pressure gradients cause the bootstrap current which modifies the q profile so that the shear typically becomes locally negative at the LFS where the ballooning modes are concentrated. This means that on a flux surface with varying sign of s_{loc} along the poloidal angle, an increasing average global magnetic shear could just mean that the negative part of s_{loc} is becoming less negative, and the plasma is becoming more ballooning unstable. In both plasma regions, in the first stability the normalised pressure gradient is destabilising the plasma for ballooning modes. At low enough global shear, at one point the increasing α ensures that the s_{loc} is negative at the LFS, and further increasing of α only further stabilises the plasma by making s_{loc} at the LFS more negative. This way the operational point enters the second stability region.

Therefore, if the pedestal middle is located in the second stable region, higher pressure gradients are achievable and the plasma confinement is improved. In this case, the pressure gradient is not limited by the local infinite-n stability, but instead finite α follows from global finite-n effects. Access to the second stable region is only possible due to the Shafranov

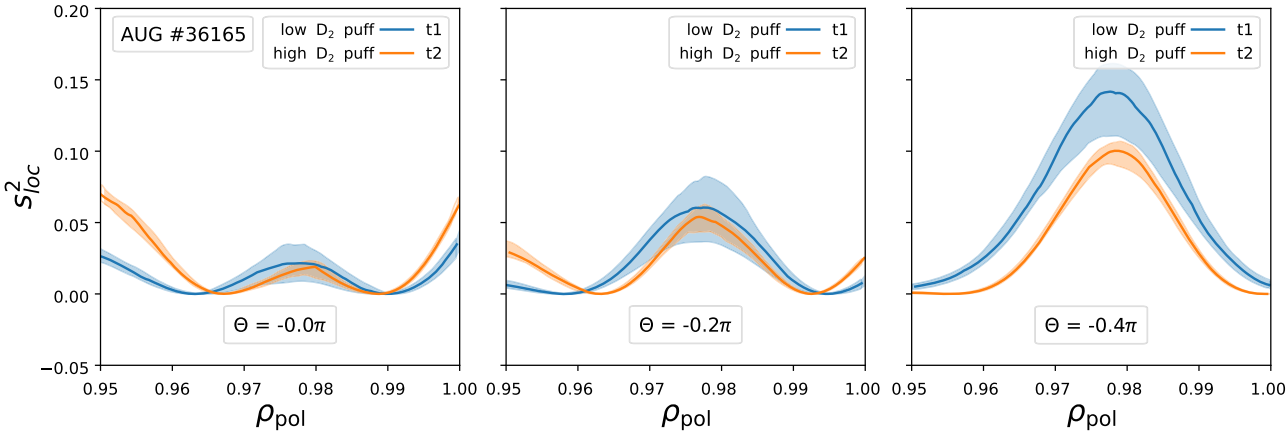

Figure 4. Local magnetic shear of discharge #36165 at the LFS for three poloidal angles relative to the LFS midplane: 0, -0.2π and -0.4π. for the low fuelling (blue) and high fuelling (orange). The full line represents the temporal median, and the shaded area the 95% of the temporal variation for the analysed 100 ms.

shift, which is causing the asymmetry of the magnetic flux surfaces and opens the passage between the first and the second stability.

We initially test the position of the operational point in the s–α diagram for discharge #36165 (figure 5). HELENA creates a grid by artificially varying the current density and the pressure gradient around the experimental point, here taken to be values of s and α at $\rho = 0.98$ in the middle of the marked time windows. For each point on the grid, the equilibrium is newly evaluated and a value of F_{marg} is calculated, plotted as a colour map (blue is stable; red is unstable). Low and high gas puff time points are shown in figures 5(a) and (b), respectively. The ballooning stability limit $F_{\text{marg}} = 1$ is marked as a full line in (b).

The operational point, marked as a black triangle, sits in the second stable region. In the low fuelling phase it is further away from the stability limit (figure 5(a)), but as the average global magnetic shear increases, it moves closer to the limit. Simultaneously, the β_N decreases by 10% which affects the Shafranov shift and consequently moves the ideal ballooning stability boundary towards lower values of s and α. Both effects contribute to reduced distance between the operational point and the stability limit.

The shift of the limit due to the changes in Shafranov shift and the location of the operational point in the s–α space has been investigated for all four discharges. Figure 7 shows a comparison of high fuelling (orange) and low fuelling (blue) at the pedestal bottom (a) and the pedestal middle (b) for all four discharges. Because $F_{\text{marg}} = 1$ is not always visible in the scan (e.g. figure 5(a)) an arbitrary slightly higher value of $F_{\text{marg}} = 1.15$ is taken as a limit. Taking a higher stability limit is also consistent with the fact that F_{marg} is an ideal ballooning stability factor, and it is known that in resistive plasmas the growing rates are higher [30, 31]. Different line and marker styles represent different discharges.

At the pedestal bottom ($\rho = 0.99$) all operational points in the high gas puff phases (orange) are inside the chosen stability limit. For all four discharges, the phases with the low gas puff have lower magnetic shear and slightly higher pressure gradient, moving them towards the second stable region. This difference is reminiscent of the small changes in shape or density required to access the QCE regime in experiments [6]. Nevertheless, the operational points still stay either inside or very close to the taken stability limit of $F_{\text{marg}} = 1.15$.

In the middle of the pedestal, at $\rho = 0.98$, the operational points are mostly located in the second stable region, except for the high gas puff phase of the high q discharge (#37161), which lies in the transition region between first and second stability. Similarly to the pedestal bottom, a low gas puff decreases the shear and stabilises the plasma against ideal ballooning modes. The stabilising effect of α ensures that the ideal ballooning modes do not restrict the growth of the pressure gradient at the pedestal middle, but instead the gradient can grow until it balances the heat and particle sources, or it is limited by another mechanism.

In the low fuelling phases, the ballooning stability limit is moving towards higher values of s and α. This effect is expected since the plasma generally has higher values of β_N in time windows where less gas is being puffed, which increases the Shafranov-shift, resulting in a larger ballooning stable region at low magnetic shear [32].

In figure 7 it is demonstrated that second stability allows higher normalised pressure gradients, which is beneficial for the confinement. Further influence on the confinement is investigated by analysing the time traces of ballooning stability factor F_{marg}.

3.3. Time evolution and confinement

Figure 8 shows time traces of the radial profiles of the marginal ballooning stability factor F_{marg} (colour map) and total D_2 gas puff (white line) in the top panels and the confinement factor $H_{98(y,2)}$ in the bottom panels. The level of noise in $H_{98(y,2)}$ indicates the occurrence of ELMs. The y axis in the top panels represents the normalised poloidal radius ρ_{pol}, blue coloured regions are ballooning stable and yellow ones are ballooning unstable. The discharges reach their final high shape at 3 s for

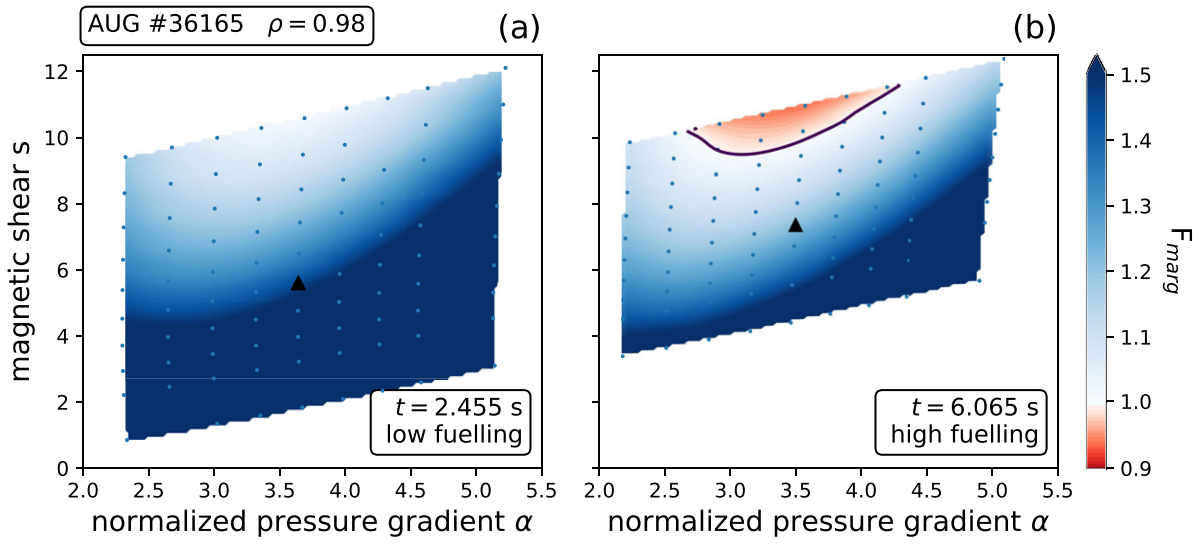

Figure 5. s–α diagrams for (a) low fuelling and (b) high fuelling for #36165. Blue contours represent marginally ballooning stable regions and red marginally ballooning unstable regions, the full line is the ballooning stability limit where $F_{\text{marg}} = 1$. Operational points are marked with black triangles.

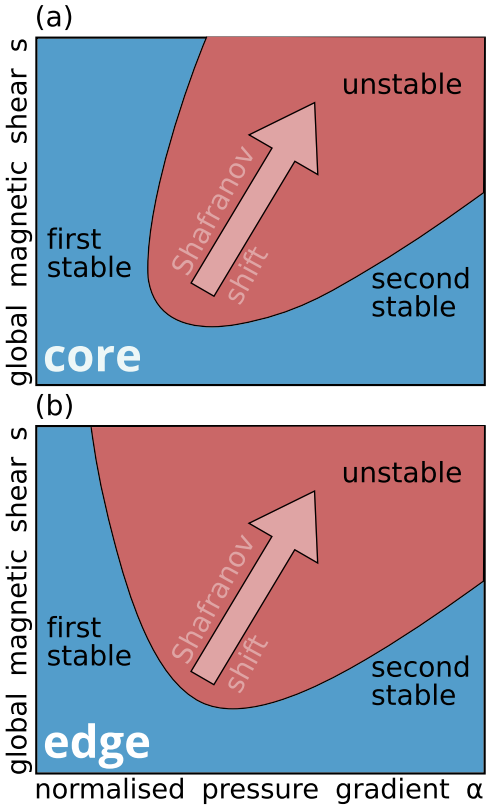

Figure 6. Sketch of s–α diagram. The typical stability regions for the core are shown in (a) and for the edge in (b). [29] John Wiley & Sons. Copyright © 2015 Wiley-VCH Verlag GmbH & Co. KGaA.

#35562 (a) and at 2 s for #36080 (b), #36165 (c) and #37161 (d).

In the high fuelling phase of the low q discharge (a), the pedestal is characterised by top and bottom which are very close to the ballooning stability limit, while the pedestal middle is more stable. After 4.5 s when the gas puff is reduced, the whole pedestal region becomes slightly narrower and more ideal ballooning stable. In this discharge, at 4 s additionally to gas puff, the plasma is fuelled by pellets. This leads to reduced confinement, which is restored after the drop in gas puff at 4.7 s. In discharge #36080 with the stepwise decrease in D_2 puff (figure 8(b)), in the first phase, the plasma is in the QCE regime. After the first step in fuelling at 2.5 s, ELMs appear stronger and $H_{98(y,2)}$ increases by ∼5%. After the second step at 4 s the pedestal region is broader, the middle of the pedestal is second stable, as discussed above, and the confinement rises further.

In the discharge with the stepwise increase in D_2 puff (figure 8(c)) similar observations can be made in reversed order. In the first phase, there are two distinct unstable regions at the pedestal top and bottom. As ELMs weaken after 4 s there is still a more stable pedestal middle and the confinement remains unchanged. In the last step, from 5 s on there are no large ELMs and the confinement factor $H_{98(y,2)}$ decreases by 5%, while the unstable regions at the pedestal top and bottom get closer together and the pedestal middle closer to the ballooning stability limit.

Figure 8(d) shows discharge #37161 with the D_2 puff reduction to zero between 4 s and 5 s. In the high puff phases there are no ELMs and the whole pedestal is close to the ballooning stability limit. In this discharge the confinement is low ($H_{98(y,2)} \approx 0.8$), since the pressure gradient is ballooning limited as shown in the previous section (figure 7). As the fuelling is reduced to 0 at 4 s, the stable region in the middle of the pedestal appears, together with larger ELMs and a pronounced increase of approximately 15% in $H_{98(y,2)}$.

The ideal ballooning stability analysis of high triangularity AUG discharges has shown that the small ELMs can be observed when the pedestal bottom is close to the ballooning stability limit. For good confinement, it is also crucial for the pedestal middle to be in the second stable region, where the maximum achievable pressure gradient is not limited by the

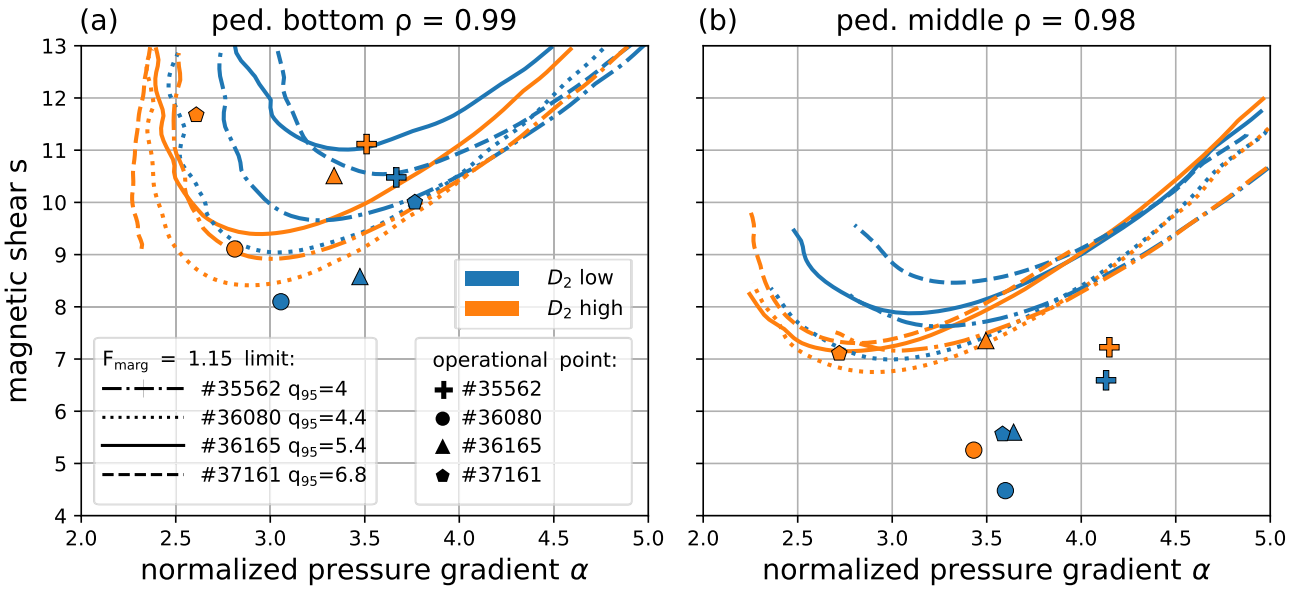

Figure 7. s–α diagram at 0.99 (*a*) and 0.98 (*b*) for four different discharges with D_2 puff variation. Ballooning stability limit is taken to be $F_{\text{marg}} = 1.15$. Colours mark different gas puff levels, where blue is low and orange high gas puff phase. Line styles and markers represent different discharges.

ballooning instability. In the following section, the previously described analysis has been carried out on a set of simulated ITER profiles in order to test if similar ballooning stability conditions in the pedestal can be met.

4. ITER

The set of ITER profiles has been constructed using the following method: a scan of the gradient length of electron density $n_e/\nabla n_e$ and electron temperature $T_e/\nabla T_e$ was produced (figure 9). The electron density at the pedestal top was fixed to be 60% of the Greenwald density limit, that is 6.8×10^{19} m^{-3}, its gradient was varied and the resulting separatrix density varies between 1.5×10^{19} m^{-3} and 3.5×10^{19} m^{-3}.

A set of varying electron temperature profiles was made for each electron density gradient length. On each combination of T_e and corresponding n_e profiles, assuming that $T_i = T_e$, a peeling ballooning analysis was performed with code MISHKA, with the toroidal mode number ranging from 5 to 40. The combination of profiles which is peeling ballooning limited is taken to form a grid of different electron temperature and density gradient lengths. From this grid, the pressure is calculated, again assuming that $T_i = T_e$ and used as an input for HELENA. The second input profile is the current density, consisting of the Ohmic current and the bootstrap current in the pedestal, and a parabolic profile shaped such that $q_{\text{axis}} = 1$ and $I_p = 15$ MA. The bootstrap current is calculated from the profiles taken from the constructed $n_e/\nabla n_e$ and $T_e/\nabla T_e$ grid. Finally, a high triangularity ITER plasma boundary was used as the third input. Two examples of calculated s, α and F_{marg} profiles, are shown in figure 10. The profile with a higher pedestal pressure (blue) shows a distinct drop in the global magnetic shear s (*a*), which indicates strong impact of negative local shear in the region of the strongest pressure gradient. This can also be observed in the α profiles marked with blue in (*b*): at the pedestal top and bottom critical and experimental α values are converging, and at the pedestal middle α_{crit} is higher than α_{exp}. Therefore, the profile of F_{marg} (*c*) takes the characteristic shape observed in AUG small ELM discharges (figure 3).

Conversely, the example with low pedestal pressure (orange) has a radially steadily increasing global shear s throughout the pedestal (*a*), resulting in a flattened α_{crit} profile (*b*) and an F_{marg} that is stable at the far plasma edge ($0.99 \lesssim \rho \lesssim 1$).

In the analysed database, 7 out of 36 profiles have an F_{marg} profile that is comparable to the case shown in orange (figure 10) and their confinement is rather poor, with the pressure varying between 58 kPa and 78 kPa at $\rho = 0.96$.

This implies that for the analysed profiles, firstly, access to the second stability is necessary for achieving high pressures in the core of the plasma. Secondly, the access to the second stability is enabled by low global s and at the same time high pressure gradients that drive the bootstrap current. Consequently, the q profile is modified in the region of the pedestal middle, such that negative local shear is achieved, that is, the operational point lies in the second stable region.

The shown blue example is one of the remaining 29 profiles that show exactly such behaviour: their pressure gradients are higher, the pedestal top and the pedestal bottom are unstable, and the pedestal middle is second stable. For these cases, two new quantities are defined, and shown in figure 10(*c*): $\min(F_{\text{marg}})$ is the minimum of the stability factor at the pedestal bottom and $\max(F_{\text{marg}})$ at the maximum at the pedestal middle.

In figure 11 $\min(F_{\text{marg}})$ is plotted on the x-axis, $\max(F_{\text{marg}})$ is plotted on the y-axis and the colour code shows the value of pressure at $\rho = 0.96$ as an indicator of the confinement.

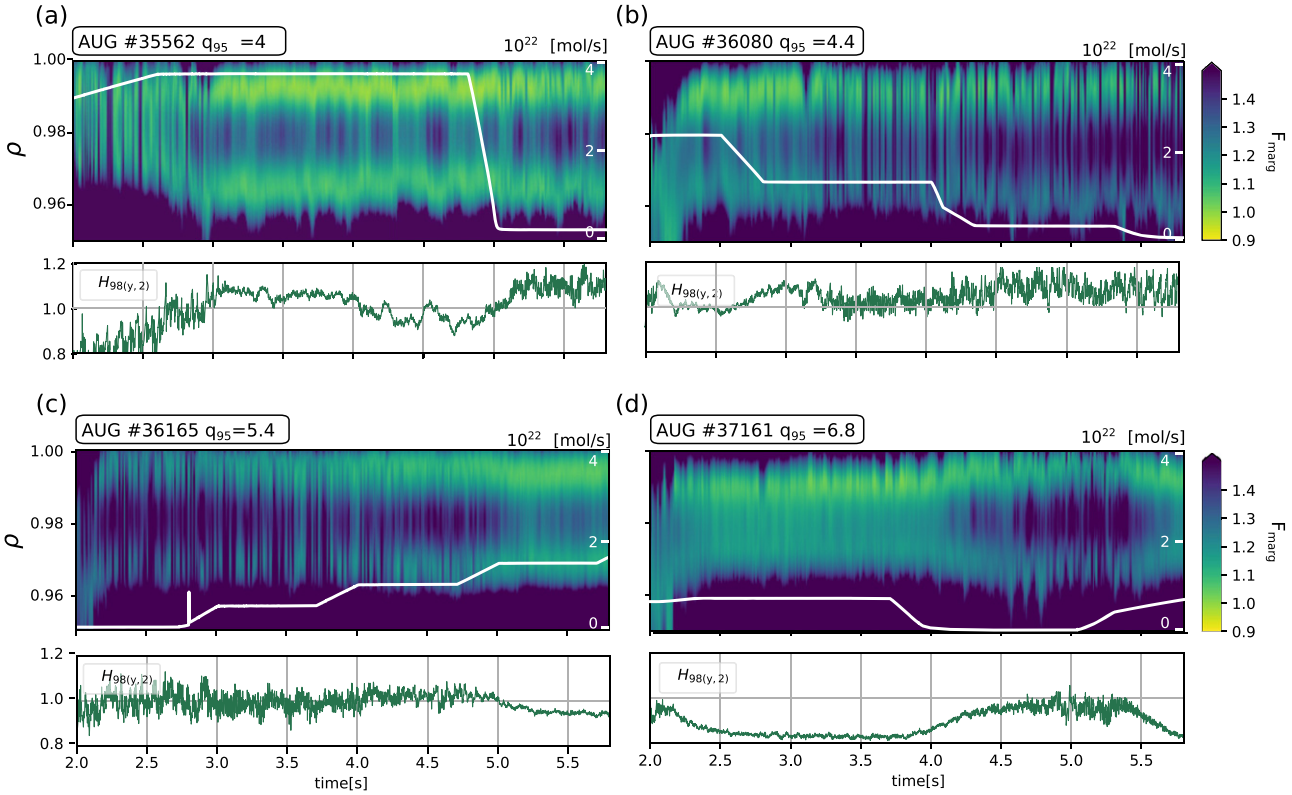

Figure 8. Time traces of ballooning stability factor F_{marg} in the plasma edge are depicted in top panels as a colour map, where blue represents ballooning stable and yellow ballooning unstable regions. The white line is the D_2 puff fuelling level, with its numeric values shown on the right side. On the bottom panels confinement factor $H_{98(98,2)}$ is shown. The discharge with high plasma current is in (*a*), discharges with medium plasma current are in (*b*) and (*c*) and the discharge with low plasma current in (*d*).

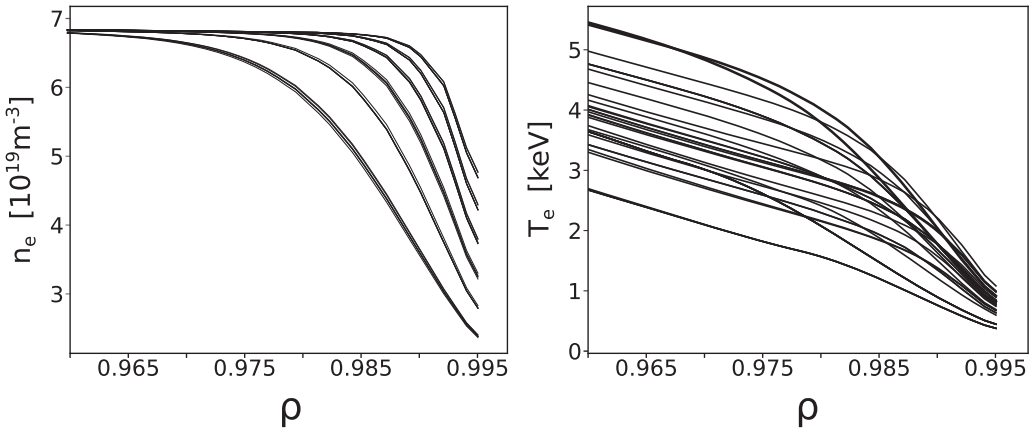

Figure 9. Modelled electron density (*a*) and temperature (*b*) pedestal profiles up to $\rho = 0.995$ used as input for the HELENA calculations of possible ITER profiles and the calculations of the current density.

This plot shows that in the performed scan, better confinement (light green and yellow) is achieved when the pedestal bottom is closer to the ballooning stability limit, that is $\min(F_{\mathrm{marg}}) \lesssim 1.05$.

For the higher pedestal top pressure values (light green and yellow), $\max(F_{\mathrm{marg}})$ varies more significantly. This indicates a larger operational space regarding the ideal ballooning stability of the pedestal middle.

If an analogy is to be drawn from the previously shown experimental results from AUG, fine-tuning the pedestal middle could make it possible to find an operational point that has good confinement and no type-I ELMs. However, one should note that this is an ideal analysis, and therefore it is not certain if the same level of instability would cause enough transport to suppress the type-I ELMs and enable the QCE regime. The results of the linear ideal ballooning analysis are supportive of the possibility to achieve the QCE regime in ITER, a certain projection can only follow from further studies using global stability analysis and non-linear modelling.

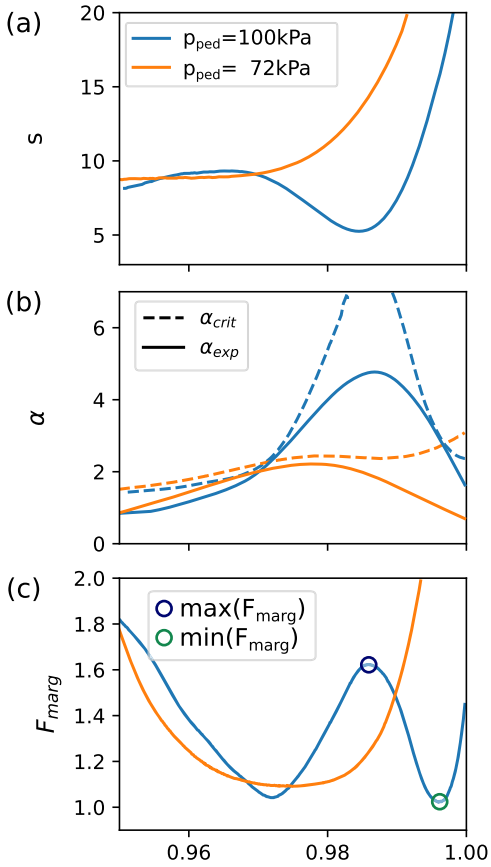

Figure 10. Radial profiles of global magnetic shear s (a), critical α (dashed line) and experimental α (full line) in (b) and ballooning stability factor F_{marg} in (c) of two example cases from the ITER scan: one with higher pedestal pressure (blue) and one with lower pedestal pressure (orange). The most stable point in the pedestal middle is marked as max(F_{marg}) and the most unstable point at the pedestal bottom is marked as min(F_{marg}).

5. Discussion and conclusions

In [6] it has been experimentally demonstrated that small ELMs have a very local nature, and it has been suggested that they are caused by radially narrow ballooning modes close to the separatrix. As shown in this analysis, at the pedestal bottom, the plasma is indeed very close to the ballooning stability limit and as small ELMs become more dominant, the plasma is more unstable in the region between $\rho = 0.99$ and $\rho = 1$.

Although this is the most ballooning unstable region in the pedestal, the rest of the pedestal also shows closeness to the ballooning stability limit, to a somewhat lesser degree.

A specific shape of the ballooning stability factor F_{marg} has been observed in all AUG discharges presented in this analysis. F_{marg} has lower values at the pedestal top and bottom and higher values in the pedestal middle. This is because of the strong stabilisation by the local magnetic shear s_{loc} in the pedestal middle at the LFS, where the ballooning modes are concentrated. Here the local shear becomes negative, but because its square is stabilising, only its absolute value has an influence. However, it implies that the local shear crosses zero twice, where it therefore has no stabilising effect. The zero crossing is at different radial positions for different poloidal angles at the LFS; nevertheless, it is always in the region of the pedestal top and the pedestal bottom. There is a clear correlation between the pedestal width and the locations of the two zero shear crossings, when different phases of the discharges are compared. One explanation for the type-I ELM suppression is that in the high gas puff phases the pedestal is narrower, making it less prone to the peeling ballooning instability, commonly thought to cause the onset of the type-I ELMs. If the ballooning modes which are located at the pedestal top cause enough transport, they could limit the widening of the pedestal. Controlling at which radial position the local shear crosses zero could therefore be a way to fix the pedestal width before the onset of the type-I ELMs. However, more dedicated research regarding the causality between s_{loc} and the pedestal width needs to be done in order to further test this hypothesis.

The normalised pressure gradient α, which is the drive for the modes, has only been significantly influenced in the low current discharge. The parameter that varied more strongly with the fuelling changes was the magnetic shear; this is because the gas puff influences the equilibrium in multiple ways. It shifts the effective position of the pedestal outwards, which has a strong impact on the pedestal stability and instead of increasing, actually lowers the pedestal electron pressure [25]. The increase in density is often compensated by the decrease in temperature, resulting in higher collisionality. This decreases the bootstrap current, which affects the equilibrium. Particularly, the changes in the q profile directly influence the magnetic shear. As shown in the section 3.2, due to the increased pressure in the low puff phases the Shafranov shift is stronger, moving the ideal ballooning stability limit towards higher values of s and α.

This demonstrates a rather complex relationship between the instability drive—the normalised pressure gradient α and the stabilising factor—the magnetic shear s. Still, varying the shape and the fuelling changes these two parameters consistently. It is then possible to achieve an F_{marg} profile where the transport caused by the ballooning modes is high enough to suppress the type-I ELMs, but not too high to significantly degrade the confinement. The requirement for good confinement is the second stability access in the middle of the pedestal, once again underlining the importance of the local magnetic shear.

In this work, we have analysed four AUG discharges with different safety factor q and varying fuelling steps. In each discharge, two phases have been compared: the low gas fuelling phases which are dominated by the large lower frequent type-I ELMs and the high puff fuelling phases that are in the QCE regime. We have found that increasing the gas puff changes not only the pressure gradient, but also significantly modifies the equilibrium. The changes in α and s result in a plasma that is very close to the ideal ballooning stability limit at the pedestal bottom, just inside the separatrix.

Based on this analysis only it cannot be exactly predicted how the optimal F_{marg} profile looks like for different varying plasma parameters, especially so because we do not consider the mode numbers, resistivity or possible non-linear effects.

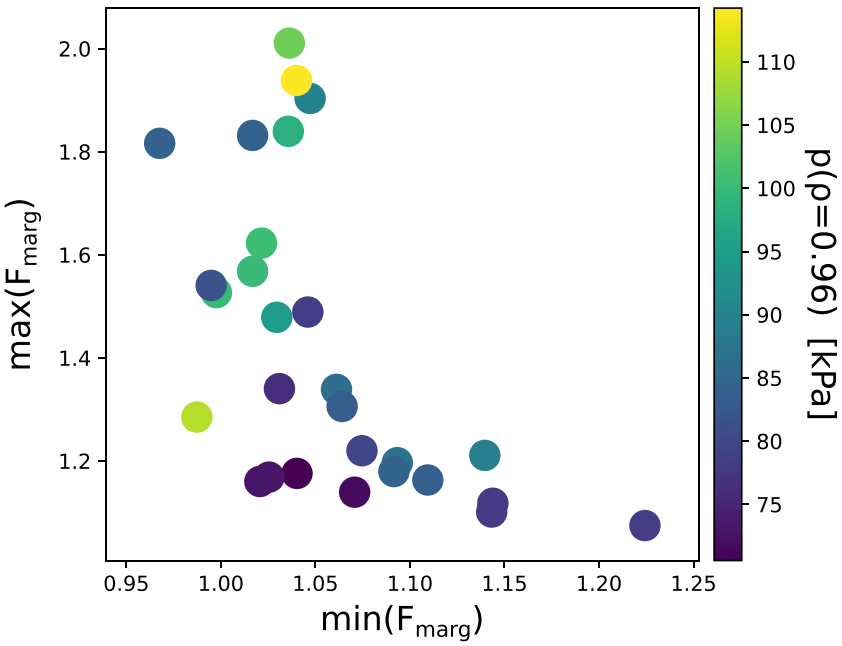

Figure 11. The local F_{marg} maximum in the pedestal middle plotted against the local F_{marg} minimum at the pedestal bottom. Colour code shows the value of the pressure at $\rho = 0.96$ (yellow—higher pressure, blue—lower pressure).

The same is true for the set of possible ITER profiles. However, the findings are supportive of the ballooning model for small ELMs and motivate further research of the role of the ballooning modes in the QCE regime, and the accessibility of this regime in the future fusion devices.

Acknowledgments

This work has been carried out within the framework of the EUROfusion Consortium, funded by the European Union via the Euratom Research and Training Programme (Grant Agreement No. 101052200—EUROfusion). Views and opinions expressed are however those of the author(s) only and do not necessarily reflect those of the European Union or the European Commission. Neither the European Union nor the European Commission can be held responsible for them. The authors acknowledge the TU Wien Bibliothek for financial support through its Open Access Funding Program.

ORCID iDs

L. Radovanovic https://orcid.org/0000-0002-1311-0482
M. Dunne https://orcid.org/0000-0002-5259-9970
G. Harrer https://orcid.org/0000-0002-1150-3987
M. Faitsch https://orcid.org/0000-0002-9809-7490
F. Aumayr https://orcid.org/0000-0002-9788-0934

References

[1] Wagner F. *et al* 1982 *Phys. Rev. Lett.* **49** 1408–12
[2] Campbell D (Collaborators I) 2012 (San Diego, USA October 8–13, 2012) (https://www-pub.iaea.org/MTCD/Meetings/PDFplus/2012/cn197/cn197_Programme.pdf) *Proc. 24th Int. Atomic Energy Agency Conf. Fusion Energy ITR/P1-18*
[3] Zohm H. *et al* 2013 *Nucl. Fusion* **53** 073019
[4] Loarte A. *et al* 2007 *Phys. Scr.* **2007** 222
[5] Eich T. *et al* 2013 *Nucl. Fusion* **53** 093031
[6] Harrer G.F. *et al* 2018 *Nucl. Fusion* **58** 112001
[7] Stober J., Maraschek M., Conway G.D., Gruber O., Herrmann A., Sips A.C.C., Treutterer W. and Zohm H. 2001 *Nucl. Fusion* **41** 1123–34
[8] Wolfrum E. *et al* 2011 *Plasma Phys. Control. Fusion* **53** 085026
[9] Sartori R. *et al* 2004 *Plasma Phys. Control. Fusion* **46** 723–50
[10] Oyama N. *et al* 2005 *Nucl. Fusion* **45** 871–81
[11] Stober J. *et al* 2005 *Nucl. Fusion* **45** 1213–23
[12] Saibene G. *et al* 2005 *Nucl. Fusion* **45** 297–317
[13] Kirk A. *et al* 2011 *Plasma Phys. Control. Fusion* **53** 095008
[14] Faitsch M., Eich T., Harrer G.F., Wolfrum E., Brida D., David P., Griener M. and Stroth U. 2021 *Nucl. Mater. Energy* **26** 100890
[15] Griener M. *et al* 2020 *Nucl. Mater. Energy* **25** 100854
[16] Snyder P.B. *et al* 2002 *Phys. Plasmas* **9** 2037–43
[17] Saarelma S., Günter S., Kiviniemi T., Kurki-Suonio T. and ASDEX Upgrade Team 2002 *Contrib. Plasma Phys.* **42** 277–82
[18] Dickinson D., Roach C.M., Skipp J.M. and Wilson H.R. 2014 *Phys. Plasmas* **21** 010702
[19] Bokshi A., Dickinson D., Roach C.M. and Wilson H.R. 2016 *Plasma Phys. Control. Fusion* **58** 075011
[20] Eich T., Goldston R.J., Kallenbach A., Sieglin B., Sun H.J. and ASDEX Upgrade Team and Contributors J 2018 *Nucl. Fusion* **58** 034001
[21] Suttrop W. 2000 *Plasma Phys. Control. Fusion* **42** A1–A14
[22] Konz C. and Zille R. 2007 *Manual* (Garching: Max Planck Institute for Plasma Physics)
[23] Hujismans G., Goedbloed J.P. and Kerner W. 1991 *Int. J. Mod. Phys.* C **2** 371–6
[24] Fischer R., Fuchs C.J., Kurzan B., Suttrop W. and Wolfrum E. 2010 *Fusion Sci. Technol.* **58** 675–84
[25] Dunne M.G. *et al* 2017 *Plasma Phys. Control. Fusion* **59** 014017

[26] Fischer R. *et al* 2016 *Fusion Sci. Technol.* **69** 526–36
[27] Galvão R.M.O. and Rem J. 1981 *Comput. Phys. Commun.* **22** 399–402
[28] Carthy P.J.M. 2013 *Plasma Phys. Control. Fusion* **55** 085011
[29] Zohm H. 2015 *Magnetohydrodynamic Stability of Tokamaks* (New York: Wiley)
[30] Moore R.W., Dominguez R.R. and Chu M.S. 1985 *Nucl. Fusion* **25** 1575–91
[31] Zehrfeld H.-P. and Grassie K. 1988 *Nucl. Fusion* **28** 891–8
[32] Connor J.W., Ham C.J. and Hastie R.J. 2016 *Plasma Phys. Control. Fusion* **58** 085002